



Band Structures Extending to Very High Spin in ^{126}Xe

C. Rønn Hansen, G. Sletten, G.B. Hagemann, B. Herskind, D.R. Jensen, P. Bringel, C. Engelhardt, H. Hûbel, A. Neusser-Neffgen, A.K. Singh, et al.

► To cite this version:

C. Rønn Hansen, G. Sletten, G.B. Hagemann, B. Herskind, D.R. Jensen, et al.. Band Structures Extending to Very High Spin in ^{126}Xe . *Physical Review C*, 2007, 76, pp.034311. 10.1103/PhysRevC.76.034311 . in2p3-00141618

HAL Id: in2p3-00141618

<https://hal.in2p3.fr/in2p3-00141618>

Submitted on 13 Apr 2007

HAL is a multi-disciplinary open access archive for the deposit and dissemination of scientific research documents, whether they are published or not. The documents may come from teaching and research institutions in France or abroad, or from public or private research centers.

L'archive ouverte pluridisciplinaire **HAL**, est destinée au dépôt et à la diffusion de documents scientifiques de niveau recherche, publiés ou non, émanant des établissements d'enseignement et de recherche français ou étrangers, des laboratoires publics ou privés.

Band Structures Extending to Very High Spin in ^{126}Xe

C. Rønn Hansen, G. Sletten^{1,*}, G.B. Hagemann, B. Herskind, and D.R. Jensen
Niels Bohr Institute, Blegdamsvej 17, DK-2100 Copenhagen, Denmark. and
¹*GANIL, BP 55027, F-14076 Caen Cedex 5, France.*

P. Bringel, C. Engelhardt, H. Hübel, A. Neußer-Neffgen, and A.K. Singh
Helmholtz-Institut für Strahlen- und Kernphysik,
Universität Bonn, Nußallee 14-16, D-53115 Bonn, Germany.

M.P. Carpenter, R.V.F. Janssens, T.L. Khoo, and T. Lauritsen
Physics Division, Argonne National Laboratory, Argonne, IL 60439, USA.

P. Bednarczyk, T. Byrski, and D. Curien
IPHC-DRS, ULP, CNRS, IN2P3, B.P. 28, F-67037 Strasbourg, France.

G. Benzoni, A. Bracco, F. Camera, and S. Leoni
Dipartimento di Fisica and INFN, Sezione di Milano, I-20133 Milano, Italy.

R.M. Clark and P. Fallon
Lawrence Berkeley National Laboratory, Ca 94720 Berkeley, USA.

A. Korichi and J. Roca
CSNSM, F-91406 Orsay, F-91406 Orsay Cedex, France.

A. Maj
Niewodniczanski Institute of Nuclear Physics, ul. Radzikowskiego 152, 31-342 Krakow, Poland.

J.N. Wilson
IPN Orsay, F-91406 Orsay Cedex, France.

J.C. Lisle
University of Manchester, Shuster Laboratory, Brunswick str. Manchester M13 9PL, UK.

T. Steinhardt and O. Thelen
Institut für Kernphysik, Universität zu Köln, D-50937 Köln, Germany.

S.W. Ødegård
Department of Physics, University of Oslo, PB 1048 Blindern, N-0316 Oslo, Norway.
(Dated: April 12, 2007)

High spin states in ^{126}Xe have been populated in the $^{82}\text{Se}(^{48}\text{Ca}, 4n)^{126}\text{Xe}$ reaction in two experiments, one at the VIVITRON accelerator in Strasbourg using the Euroball detector array, and a subsequent one with ATLAS at Argonne using the Gammasphere Ge-detector array. Levels and assignments made previously for ^{126}Xe up to $I = 20$ have been confirmed and extended. Four regular bands extending to a spin of almost $I = 60$, which are interpreted as two pairs of signature partners with opposite parity, are identified for the first time. The $\alpha = 0$ partner of each pair is connected to the lower-lying levels, while the two $\alpha = 1$ partners remain floating. A peak-shape analysis of transitions in the strongest populated $(\pi, \alpha) = (-, 0)$ band provides a value of $5.2_{0.5}^{0.4}$ b for the transition quadrupole moment, which can be related to a minimum in the potential-energy surface calculated by the Ultimate Cranker cranked shell model code at $\epsilon \approx 0.35$ and $\gamma \approx 5^\circ$. The four lowest bands calculated for this minimum compare well with the two signature pairs experimentally observed over a wide spin range. A sharp upbend at $\hbar\omega \sim 1170$ keV is interpreted as a crossing with a band involving the $j_{15/2}$ neutron orbital, for which pairing correlations are expected to be totally quenched. The four long bands extend to within ~ 5 spin units of a crossing with an yrast line defined by calculated hyperdeformed transitions and will serve as important stepping stones into the spin region beyond $60 \hbar$ for future experiments.

PACS numbers: 23.20.Lv, 23.20.En, 27.60.+j, 29.30.-h, 21.60.-n

I. INTRODUCTION

Nuclei in the $A = 120 - 130$ mass region are considered transitional with regard to their shape at low and high angular momentum. The rotational motion leads to Coriolis-induced alignment effects which in the present case are governed by the $h_{11/2}$ unique parity intruder subshell for both neutrons and protons. A most conspicuous feature of these nuclei is their γ softness and the large susceptibility to polarisation effects from the excitation of individual quasiprotons and quasineutrons. The alignment of the protons tends to drive the nuclear shape towards prolate deformation, while the alignment of neutrons induces an oblate shape. Already the presence of a single $h_{11/2}$ neutron will drive the nucleus towards oblate deformation, whereas additional neutrons have only a small effect [1].

Seiffert et al. [2] have established 13 band structures in ^{126}Xe up to a spin of about $20 \hbar$ based on experiments with the $^{116}\text{Cd}(^{13}\text{C}, 3n)$ and $^{123}\text{Te}(\alpha, n)$ reactions. Firm assignments of spin and parity to the majority of the levels were made on the basis of angular distribution and linear polarisation measurements of the γ rays and comparison of level properties to calculations within the $O(6)$ limit of the interacting boson model and the cranked shell model [2].

Theoretical calculations show that the tendency towards non-axial symmetry of these nuclei gives rise to a substantially smaller fission width at high spin [3]. Therefore, they provide an opportunity for populating levels at extreme spins. A hyperdeformed (HD) minimum at $I \leq 70$ is predicted in ^{126}Xe by liquid drop model calculations [4] with a fission barrier of several MeV at the highest spins. Similarly, a deep prolate minimum and a high barrier against fission at $\epsilon_2 \approx 0.95$ is found in calculations with the Ultimate Cranker (UC) code [5]. These predictions have been the motivation for the two major experimental campaigns which are reported in this work. Separate accounts of the efforts to identify ridges corresponding to hyperdeformation in ^{126}Xe are presented in refs. [6, 7]. In the present paper, we shall describe the discrete-line spectroscopy which takes advantage of the assignments previously given in ref. [2] and extends the spectroscopy considerably. An outstanding feature of the level structure is the remarkable regularity, which appears beyond spin 20, where four newly identified bands extend almost to spin 60 at more than 42 MeV of excitation.

II. EXPERIMENTAL DETAILS

Two experiments, both with the reaction $^{82}\text{Se}(^{48}\text{Ca}, xn)^{130-x}\text{Xe}$ have been performed using major Ge-detector arrays. The first experiment, hereafter referred to as Xe1, was carried out at the VIVITRON at Strasbourg where $1.9 \cdot 10^9$ events were detected by the Euroball array [8] with the Ge-fold selection $\text{Ge}_{sup} \geq 3$. The incident beam energy was 195 MeV, entering through the Au backing of the Se target, and was reduced to about 190 MeV at mid-target. The beam intensity was less than 1 pA. The second experiment, hereafter referred to as Xe2, was performed at the ATLAS accelerator at ANL and γ -ray coincidences were measured with the Gammasphere array [9]. The beam energy was 205 MeV incident on the target and about 200 MeV at mid-target. A total of $2.8 \cdot 10^9$ events with a fold selection $\text{Ge}_{sup} \geq 5$ was recorded. In both experiments the γ -ray coincidence events were stored on magnetic tape.

Selenium is a chemical homologue of sulfur and is far from an ideal target for heavy-ion bombardment. Self-supporting foils for use with heavy-ion beams cannot be produced and for supported films, the tendency for sublimation and melting, even at about 200°C , requires special care. The targets with a thickness of $500 \mu\text{g}/\text{cm}^2$ were produced by evaporation of 98.8% enriched ^{82}Se onto a $500 \mu\text{g}/\text{cm}^2$ Au foil and by finally evaporating a $80 \mu\text{g}/\text{cm}^2$ Au protecting layer onto the Se. These targets could successfully withstand beam intensities up to about 1 pA used in the Xe1 experiment. In the Xe2 experiment, however, where up to 4 pA were used, the beam was slightly defocussed and wobbled over the target which was mounted on four quadrants of a rotating wheel [10]. In this way a low heat deposit per unit area in the target was achieved. At the same time a continuous monitoring of the target was possible via an on-line spectrum of the trigger rate versus the coordinates of the target surface as a function of time. These targets remained undamaged after seven days of ^{48}Ca bombardment, most of the time at an intensity of 4 pA.

III. ANALYSIS AND RESULTS

The γ -ray coincidence events from both experiments were sorted into data bases on disc from which cubes and four-dimensional hypercubes were produced using the Radware software package [11]. Gated matrices for the determination of angular distributions of γ rays were built, using a combination of detectors at forward and backward

*Electronic address: sletten@nbi.dk

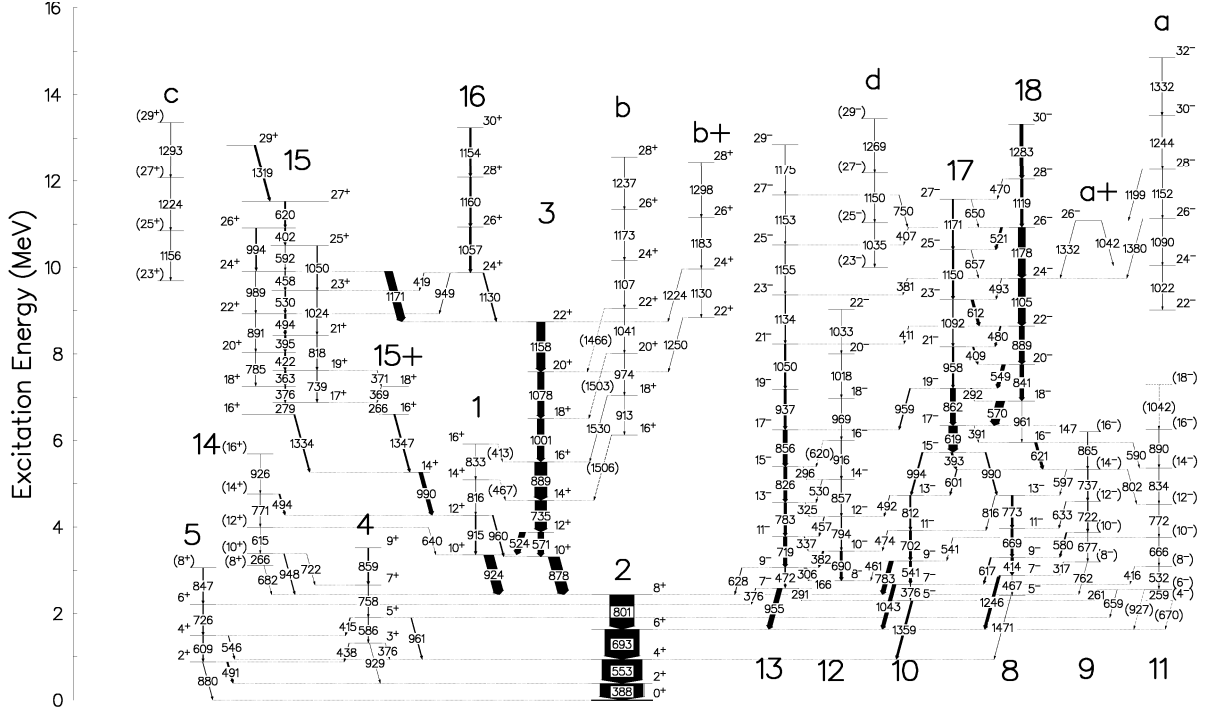


FIG. 1: Partial, low-spin level scheme of ^{126}Xe . The labelling used in ref. [2] for the previously known bands is maintained, bands 16, 17, 18, **a**, **b**, **c** and **d** are new structures identified in the present work. The widths of the arrows correspond to intensity, while transitions with less than about 20% of the 388.3 keV ground state transition are drawn as arrows with a standard width.

angles (43 crystals), against the events from angles around 90° (50 crystals) taken from the Xe2 database. The data from Xe1 were initially used to build the level scheme shown in Figs. 1 and 2, whereas the more extensive Xe2 data were used for extracting angular distributions, to disentangle difficult coincidence relationships and, finally, to facilitate the analysis of peak widths as a function of the recoil velocity v/c for the Doppler shift corrections and determination of the transition quadrupole moment for the strongest high-spin band.

The experimental data are presented in Tables I and II. Table I contain the level energies, the spin and parity assignments, the transition energies, the γ -ray intensities, the angular intensity ratios, the extracted multipole order and the $B(M1)/B(E2)$ ratios for selected cases. The R_Θ ratios given in the tables were created from two asymmetric coincidence matrices. One matrix was created with a gate list including all detectors on one axis and the detectors in the angular interval $17^\circ \leq \Theta \leq 50^\circ$ and $130^\circ \leq \Theta \leq 163^\circ$ on the other axis. The second matrix was sorted with the same gate list including all detectors on one axis and the detectors in the angular interval $70^\circ \leq \Theta \leq 130^\circ$ on the other axis. The ratios R_Θ were obtained from the intensities of the peaks,

$$R_\Theta = \frac{I_{(\text{forwd.}-\text{backwd.})}}{I_{\sim 90^\circ}}$$

This procedure has the advantage of higher statistical accuracy compared to DCO ratios. For stretched quadrupole radiation $R_\Theta = 1.40 \pm 0.04$, while for stretched dipoles $R_\Theta = 0.74 \pm 0.02$ is expected. These values are based on experimental results for transitions with multipole order determined in the work of Granderath et al. [1] and Seiffert et al. [2].

The newly observed long bands extending from the spin 20 region to very high spins are named **a**, **b**, **c** and **d**. Table

Band ID	Level energy (keV)	$I_i^\pi \rightarrow I_f^\pi$	E_γ (keV)	Intensity	R_θ	$E(\lambda)/M(\lambda)$	$B(M1)/B(E2)$ (μ_N^2/e^2b^2)
Ground band 2	388.3	$2^+ \rightarrow 0^+$	388.3	1000	1.17 ± 0.01	E2	
	941.3	$4^+ \rightarrow 2^+$	553.0	926.6 ± 29.3	1.27 ± 0.02	E2	
	1634.1	$6^+ \rightarrow 4^+$	692.8	798.0 ± 25.0	1.33 ± 0.02	E2	
	2434.7	$8^+ \rightarrow 6^+$	800.7	567.6 ± 18.2	1.39 ± 0.04	E2	
1	3359.0	$10^+ \rightarrow 8^+$	924.2	223.5 ± 7.9	1.39 ± 0.04	E2	
	4272.2	$12^+ \rightarrow 10^+$	915.1	29.9 ± 2.8	1.41 ± 0.04	E2	
		$12^+ \rightarrow 10^+$	960.1	25.8 ± 2.5	1.42 ± 0.07	E2	
	5088.0	$14^+ \rightarrow 12^+$	816.3	7.2 ± 1.3	1.39 ± 0.10	E2	
		$14^+ \rightarrow 14^+$ (466.9)	<0.2				
	5920.8	$16^+ \rightarrow 14^+$	832.8	4.3 ± 4.0	1.42 ± 0.12	E2	
		$16^+ \rightarrow 16^+$ (413.2)	<0.4				
3	3312.9	$10^+ \rightarrow 8^+$	878.3	254.7 ± 9.1	1.39 ± 0.04	E2	
	3883.5	$12^+ \rightarrow 10^+$	524.4	139.8 ± 5.7			
		$12^+ \rightarrow 10^+$	570.6	136.9 ± 5.8	1.42 ± 0.04	E2	
	4618.5	$14^+ \rightarrow 12^+$	734.8	277.3 ± 9.4	1.45 ± 0.06	E2	
	5507.6	$16^+ \rightarrow 14^+$	889.1	290.7 ± 10.2	1.42 ± 0.04	E2	
	6508.3	$18^+ \rightarrow 16^+$	1000.7	161.3 ± 5.7	1.38 ± 0.05	E2	
	7585.9	$20^+ \rightarrow 18^+$	1077.6	153.9 ± 5.6	1.37 ± 0.05	E2	
	8744.3	$22^+ \rightarrow 20^+$	1158.5	197.5 ± 7.2	1.39 ± 0.09	E2	
	9915.1	$24^+ \rightarrow 22^+$	1170.8	184.3 ± 12.6	1.40 ± 0.13	E2	
8	2412.8	$5^- \rightarrow 4^+$	1471.5	2.8 ± 1.3	0.87 ± 0.20	E1	
	2879.8	$7^- \rightarrow 6^+$	1245.9	68.5 ± 4.2	0.90 ± 0.20	E1	
		$7^- \rightarrow 5^-$	467.0	3.0 ± 1.0			
	3293.7	$9^- \rightarrow 7^-$	414.0	65.9 ± 3.0	1.37 ± 0.12	E2	
		$9^- \rightarrow 7^-$	617.1	28.9 ± 2.2			
	3962.4	$11^- \rightarrow 9^-$	669.0	60.5 ± 5.6	1.35 ± 0.12	E2	
	4734.9	$13^- \rightarrow 11^-$	773.0	51.1 ± 4.0	1.41 ± 0.10	E2	
9		$13^- \rightarrow 11^-$	816.1	6.2 ± 1.7			
	3196.6	$8^- \rightarrow 7^-$	316.9	4.8 ± 1.1			
		$8^- \rightarrow 8^+$	762.1	<0.5			
	3873.4	$10^- \rightarrow 9^-$	580.0	27.8 ± 3.4			2.0 ± 0.3
		$10^- \rightarrow 8^-$	677.0	7.2 ± 0.9			
	4595.2	$12^- \rightarrow 10^-$	721.7	22.3 ± 2.1			
		$12^- \rightarrow 11^-$	632.8	9.6 ± 1.9			0.23 ± 0.05
	5331.9	$14^- \rightarrow 12^-$	737.0	23.3 ± 4.0			
		$14^- \rightarrow 12^-$	600.8	20.2 ± 1.9			
		$14^- \rightarrow 13^-$	596.7	3.0 ± 1.2			0.71 ± 0.15
		$14^- \rightarrow 12^-$	801.7	0.8 ± 0.4			
	6198.1	$16^- \rightarrow 14^-$	865.0	14.4 ± 4.4			
10	2299.6	$5^- \rightarrow 4^+$	1358.7	51.6 ± 5.9			
	2676.9	$7^- \rightarrow 6^+$	1042.8	87.4 ± 5.6			
		$7^- \rightarrow 5^-$	376.5	8.2 ± 1.3			
	3217.5	$9^- \rightarrow 8^+$	783.1	104.0 ± 6.0			
		$9^- \rightarrow 7^-$	540.6	54.0 ± 3.4			
		$9^- \rightarrow 8^-$	460.7	3.0 ± 0.8			0.018 ± 0.005
	3919.4	$11^- \rightarrow 9^-$	702.1	59.9 ± 4.5			
		$11^- \rightarrow 10^-$	474.2	8.0 ± 0.9			0.15 ± 0.02
	4731.1	$13^- \rightarrow 11^-$	811.8	36.5 ± 2.6			
		$13^- \rightarrow 12^-$	492.3	9.1 ± 1.3			0.51 ± 0.08

Band ID	Level energy (keV)	$I_i^\pi \rightarrow I_f^\pi$	E_γ (keV)	Intensity	R_θ	$E(\lambda)/M(\lambda)$	$B(M1)/B(E2)$ (μ_N^2/e^2b^2)
11	2303.4	$(4^-) \rightarrow 6^+$	(670.3)	<0.1			0.12±0.08
	2561.3	$(6^-) \rightarrow 5^-$	261.0	2.7±0.3			
		$(6^-) \rightarrow 5^+$	658.8	2.1±0.3			
		$(6^-) \rightarrow 4^-$	259.9	1.0±0.6			
		$(6^-) \rightarrow 6^+$	(927.1)	<0.1			-
	3092.9	$(8^-) \rightarrow (6^-)$	531.7	5.2±2.1			
		$(8^-) \rightarrow 7^-$	416.2	<0.1			
	3758.8	$(10^-) \rightarrow 9^-$	541.2	5.9±2.3			
		$(10^-) \rightarrow (8^-)$	666.1	4.5±2.4			0.8±0.5
	4530.3	$(12^-) \rightarrow (10^-)$	772.0	4.1±0.7			
	5363.8	$(14^-) \rightarrow (12^-)$	833.7	2.9±0.8			
12	6255.2	$(16^-) \rightarrow (14^-)$	890.3	5.7±2.5			0.8±0.5
	(7297.5)	$(18^-) \rightarrow (16^-)$	(1042.3)	<0.3			
	2755.9	$8^- \rightarrow 7^-$	166.4	69.7±2.3		E1	1.29±0.08
	3444.5	$10^- \rightarrow 8^-$	690.1	59.6±2.5		E2	
		$10^- \rightarrow 9^-$	382.2	39.4±1.6			
	4238.5	$12^- \rightarrow 10^-$	793.9	18.4±1.4	1.39±0.08	E2	
		$12^- \rightarrow 11^-$	456.6	14.3±1.1			1.8±0.2
	5095.2	$14^- \rightarrow 12^-$	857.4	16.5±3.0	1.40±0.10	E2	
		$14^- \rightarrow 13^-$	530.0	5.4±0.8			
	6011.4	$16^- \rightarrow 14^-$	916.0	14.4±0.2	1.39±0.12	E2	
13		$16^- \rightarrow 15^-$	(620.0)	<0.3			0.71±0.17
	6981.0	$18^- \rightarrow 16^-$	969.0	10.2±1.9	1.40±0.13	E2	
	8000.1	$20^- \rightarrow 18^-$	1018.5	7.7±2.4	1.39±0.14	E2	
	9033.2	$22^- \rightarrow 20^-$	1033.1	<1.0	1.40±0.23	E2	
	2589.3	$7^- \rightarrow 6^+$	954.8	117.4±5.8	0.97±0.03	E1	1.43±0.10
		$7^- \rightarrow 6^+$	376.0	12.5±1.0		E1	
		$7^- \rightarrow 5^-$	291.3	5.7±0.8			
	3062.2	$9^- \rightarrow 8^-$	306.1	71.0±2.2			
		$9^- \rightarrow 7^-$	472.4	28.3±1.8		E2	0.59±0.04
		$9^- \rightarrow 8^+$	628.4	12.2±2.1		E1	
	3781.3	$11^- \rightarrow 9^-$	718.7	87.0±3.2		E2	
		$11^- \rightarrow 10^-$	337.3	14.9±0.8			
	4564.7	$13^- \rightarrow 11^-$	783.2	65.7±3.2	1.36±0.05	E2	0.39±0.07
		$13^- \rightarrow 12^-$	325.2	4.3±0.8			
	5391.0	$15^- \rightarrow 13^-$	826.2	82.0±3.3	1.37±0.05	E2	
		$15^- \rightarrow 14^-$	296.1	1.6±0.6			
	6246.9	$17^- \rightarrow 15^-$	856.0	99.8±4.6	1.39±0.06	E2	0.20±0.07
	7183.7	$19^- \rightarrow 17^-$	936.8	59.0±2.7	1.37±0.07	E2	
	8233.8	$21^- \rightarrow 19^-$	1050.1	42.5±2.2	1.41±0.07	E2	
	9368.0	$23^- \rightarrow 21^-$	1134.3	23.9±1.7	1.42±0.10	E2	
	10522.9	$(25^-) \rightarrow (23^-)$	1155.3	11.1±2.3	1.39±0.13	E2	2.1±1.5
	11676.7	$27^- \rightarrow 25^-$	1153.0	8.4±5.0	1.39±0.13	E2	
		$27^- \rightarrow 26^-$	749.8	5.3±2.2		(M1)	
	12850.9	$29^- \rightarrow 27^-$	1175.8	5.4±4.1	1.40±0.17	E2	

II contains the experimental results for these bands. The numbering of the bands used in ref. [2] is maintained and extended with bands 16, 17 and 18. The structure of ^{126}Xe as it appears in light- and heavy-ion induced reactions changes dramatically in the spin range around $20\hbar$, and the level scheme is, therefore, shown in two parts for clarity. Fig. 1 shows the low-spin part of the levels, and Fig. 2 contains the levels of the higher spin range. In both figures a guide to the intensity flow is given by the widths of the transition arrows, but for details we refer to Tables I and II. In the tables all intensities are given relative to the 388 keV $2^+ \rightarrow 0^+$ ground state transition. Spins and parities

Band ID	Level energy (keV)	$I_i^\pi \rightarrow I_f^\pi$	E_γ (keV)	Intensity	R_θ	$E(\lambda)$ $M(\lambda)$	$B(M1)/B(E2)$ (μ_N^2/e^2b^2)
15	6597.4	$16^+ \rightarrow 14^+$	1333.7	32.8 ± 4.0	1.39 ± 0.10	E2	9.0 ± 0.7
	6876.8	$17^+ \rightarrow 16^+$	279.4	30.5 ± 1.2	0.75 ± 0.05	(M1)	
		$17^+ \rightarrow 16^+$	265.7	13.0 ± 0.7	0.71 ± 0.04	(M1)	
	7252.7	$18^+ \rightarrow 17^+$	375.8	29.6 ± 1.4	0.73 ± 0.05	(M1)	
	7615.4	$19^+ \rightarrow 18^+$	362.6	46.1 ± 1.7	0.73 ± 0.04	(M1)	
		$19^+ \rightarrow 17^+$	739.4	18.2 ± 1.2	1.40 ± 0.09	E2	
		$19^+ \rightarrow 18^+$	370.9	6.4 ± 0.5	0.75 ± 0.05	(M1)	
		8037.8	$20^+ \rightarrow 19^+$	422.4	39.6 ± 1.5	0.73 ± 0.05	(M1)
		$20^+ \rightarrow 18^+$	785.0	7.3 ± 0.6		E2	
		8432.8	$21^+ \rightarrow 20^+$	394.9	42.8 ± 1.6	0.73 ± 0.04	(M1)
		$21^+ \rightarrow 19^+$	817.8	16.1 ± 1.7	1.41 ± 0.16	E2	
		8926.7	$22^+ \rightarrow 21^+$	493.8	44.4 ± 1.8	0.75 ± 0.05	(M1)
		$22^+ \rightarrow 20^+$	890.7	6.8 ± 1.1		E2	
		9457.2	$23^+ \rightarrow 22^+$	530.5	26.6 ± 1.2	0.78 ± 0.08	(M1)
		$23^+ \rightarrow 21^+$	1023.6	13.1 ± 1.2	1.38 ± 0.16	E2	
		9915.6	$24^+ \rightarrow 23^+$	458.4	18.0 ± 1.0	0.68 ± 0.15	(M1)
		$24^+ \rightarrow 22^+$	989.3	6.3 ± 1.0		E2	
		10507.9	$25^+ \rightarrow 23^+$	1050.4	15.6 ± 1.5	1.40 ± 0.16	
10910.2	$25^+ \rightarrow 24^+$	592.0	6.1 ± 2.6		(M1)	1.7 ± 0.7	
	$26^+ \rightarrow 25^+$	402.3	37.7 ± 1.7	0.76 ± 0.09	(M1)		
	$26^+ \rightarrow 24^+$	993.0	22.3 ± 2.4	1.38 ± 0.18	E2		
	$26^+ \rightarrow 24^+$	993.8	4.5 ± 1.3		E2		
	11530.5	$27^+ \rightarrow 26^+$	620.4	34.0 ± 4.6	0.85 ± 0.07		-
	15+	5264.0	$14^+ \rightarrow 12^+$	990.3	90.6 ± 4.9		1.42 ± 0.9
6611.0		$16^+ \rightarrow 14^+$	1347.0	37.7 ± 3.8	1.42 ± 0.18	E2	
7245.0		$18^+ \rightarrow 17^+$	369.0	4.8 ± 0.9	0.75 ± 0.05	(M1)	
16	9876.0	$24^+ \rightarrow 22^)$	1130.3	28.3 ± 1.4	1.40 ± 0.12	E2	
		$24^+ \rightarrow 23^+$	418.6	7.5 ± 0.7	0.75 ± 0.08	(M1)	
		$24^+ \rightarrow 22^+$	949.3	6.9 ± 1.2	1.44 ± 0.18	E2	
		10933.0	$26^+ \rightarrow 24^+$	1057.0	48.0 ± 3.2	1.38 ± 0.09	E2
	12093.2	$28^+ \rightarrow 26^+$	1160.2	46.3 ± 3.7	1.41 ± 0.10	E2	
	13247.3	$30^+ \rightarrow 28^+$	1154.2	42.1 ± 2.9	1.41 ± 0	E2	
17	5724.8	$15^- \rightarrow 14^-$	393.1	48.3 ± 2.4	0.92 ± 0.07	(M1)	
		$15^- \rightarrow 13^-$	993.7	35.4 ± 2.0	1.41 ± 0.17	E2	
		$15^- \rightarrow 13^-$	989.9	30.5 ± 2.0	1.38 ± 0.18	E2	
		6344.0	$17^- \rightarrow 15^-$	619.2	205.1 ± 8.0	1.39 ± 0.05	
	$17^- \rightarrow 16^-$		391.0	1.4 ± 1.7			
	7205.9	$19^- \rightarrow 17^-$	862.0	122.8 ± 4.8	1.42 ± 0.07		(M1)
		$19^- \rightarrow 18^-$	292.0	36.27 ± 1.6	0.94 ± 0.08	(M1)	
		$19^- \rightarrow 17^-$	958.6	23.7 ± 2.1	1.40 ± 0.20	E2	
		8164.0	$21^- \rightarrow 19^-$	958.1	41.8 ± 3.0	1.39 ± 0.15	E2
		$21^- \rightarrow 20^-$	409.0	36.3 ± 1.7	0.98 ± 0.10	(M1)	
		9256.2	$23^- \rightarrow 22^-$	612.1	63.2 ± 3.2		(M1)
		$23^- \rightarrow 21^-$	1092.3	25.1 ± 2.4	1.43 ± 0.21	E2	
		10406.3	$25^- \rightarrow 23^-$	1150.2	45.2 ± 3.0	1.43 ± 0.19	E2
	11577.2	$(25^-) \rightarrow (24^-)$	657.1	5.9 ± 1.6		(M1)	0.65 ± 0.18
		$27^- \rightarrow 25^-$	1171.0	40.1 ± 2.9	1.42 ± 0.17	E2	
		$27^- \rightarrow 26^-$	650.0	< 0.3		(M1)	

Band ID	Level energy (keV)	$I_i^\pi \rightarrow I_f^\pi$	E_γ (keV)	Intensity	R_θ	$E(\lambda)/M(\lambda)$	$B(M1)/B(E2)$ (μ_N^2/e^2b^2)
18	5953.0	$16^- \rightarrow 14^-$	621.1	60.5 ± 5.4			
		$16^- \rightarrow 14^-$	589.6	2.4 ± 0.5			
	6913.9	$18^- \rightarrow 17^-$	570.0	194.4 ± 7.2	0.71 ± 0.02	(M1)	
		$18^- \rightarrow 16^-$	960.6	< 0.3		E2	
	7755.0	$20^- \rightarrow 18^-$	841.1	95.3 ± 4.2	1.41 ± 0.08	E2	
		$20^- \rightarrow 19^-$	549.1	85.8 ± 3.5	0.69 ± 0.02	(M1)	1.59 ± 0.10
	8644.2	$22^- \rightarrow 20^-$	889.2	127.7 ± 5.6	1.40 ± 0.07	E2	
		$22^- \rightarrow 21^-$	480.1	30.1 ± 1.5	0.95 ± 0.08	(M1)	0.82 ± 0.07
	9749.1	$24^- \rightarrow 22^-$	1104.9	165.3 ± 5.9	1.38 ± 0.06	E2	
		$24^- \rightarrow 23^-$	492.8	7.9 ± 1.9		(M1)	1.2 ± 0.3
		$24^- \rightarrow 23^-$	381.4	6.9 ± 1.2	0.72 ± 0.05	(M1)	
	10927.3	$26^- \rightarrow 24^-$	1178.3	175.5 ± 6.0	1.40 ± 0.07	E2	
		$26^- \rightarrow 25^-$	521.0	51.8 ± 2.5		(M1)	3.5 ± 0.2
		$26^- \rightarrow 25^-$	407.0	2.0 ± 0.8			
	12046	$28^- \rightarrow 26^-$	1119.0	63.7 ± 3.1	1.42 ± 0.12	E2	
		$28^- \rightarrow 27^-$	469.5	5.5 ± 1.1		(M1)	3.5 ± 0.2
	13330.6	$30^- \rightarrow 28^-$	1283.4	87.2 ± 4.0	1.39 ± 0.13	E2	

TABLE I: Level energies, spin and parity assignments, γ -ray energy, relative intensities, angular distribution ratios R_θ (see section III), assignment of multipole order and $B(M1)/B(E2)$ ratios of transitions in bands 1 - 18. With very few exceptions, all transitions above $15 \hbar$ are newly observed in this work. For band 15, 16, 17 and 18 all transitions are new observations. The intensities are measured relative to the $388.3 \text{ keV } 2^+ \rightarrow 0^+$ groundstate transition. Closely lying and weak transitions are fitted separately, while the intensities of the stronger lines are fitted with routines of the Radware programme package [11].

Band ID	Level energy (keV)	$I_i^\pi \rightarrow I_f^\pi$	E_γ (keV)	Intensity	R_θ	$E(\lambda)/M(\lambda)$
a	10039.6	$24^- \rightarrow 22^-$	1022.0	1.8 ± 1.4	1.32 ± 0.19	(E2)
	11129.8	$26^- \rightarrow (24^-)$	1090.4	1.3 ± 1.0	1.39 ± 0.17	E2
		$26^- \rightarrow 24^-$	1378.7	1.0 ± 1.9	1.58 ± 0.45	E2
	12277.0	$26^- \rightarrow 24^-$	1152.2	3.5 ± 0.1	1.41 ± 0.12	E2
		$28^- \rightarrow 26^-$	1198.7	1.8 ± 0.6	1.42 ± 0.22	E2
	13521.4	$30^- \rightarrow 28^-$	1244.4	13.2 ± 1.9	1.41 ± 0.08	E2
	14853.4	$32^- \rightarrow 30^-$	1332.1	13.0 ± 1.0	1.41 ± 0.08	E2
	16284.8	$34^- \rightarrow 32^-$	1431.5	12.4 ± 1.3	1.44 ± 0.09	E2
	17825.5	$36^- \rightarrow 34^-$	1540.7	9.6 ± 1.0	1.42 ± 0.12	E2
	19483.7	$38^- \rightarrow 36^-$	1658.2	8.5 ± 1.2	1.44 ± 0.13	E2
	21264.8	$40^- \rightarrow 38^-$	1781.3	7.6 ± 1.1	1.42 ± 0.15	E2
	23172.1	$42^- \rightarrow 40^-$	1907.4	6.3 ± 1.0	1.41 ± 0.15	E2
	25208.9	$44^- \rightarrow 42^-$	2036.8	5.1 ± 0.9	1.40 ± 0.20	E2
	27372.4	$46^- \rightarrow 44^-$	2163.6	4.5 ± 0.8	1.37 ± 0.29	E2
	29656.2	$48^- \rightarrow 46^-$	2283.8	3.3 ± 0.5	1.40 ± 0.33	E2
	32008.1	$50^- \rightarrow 48^-$	2354.0	1.3 ± 0.3	1.50 ± 0.46	E2
	34355.0	$52^- \rightarrow 50^-$	2349.0	0.8 ± 0.3	(1.50 ± 0.46)	(E2)
	36797.0	$54^- \rightarrow 52^-$	2442.0	0.7 ± 0.2		(E2)
	39312.0	$56^- \rightarrow 54^-$	2515.0	0.4 ± 0.1		(E2)
a+	11079.5	$26^- \rightarrow 24^-$	1042	2.2 ± 0.5	(0.72 ± 0.13)	(E2)
		$26^- \rightarrow 24^-$	1332.2	2.0 ± 1.1	(1.40 ± 0.18)	(E2)
a~	32077.0	$50^- \rightarrow 48^-$	2421.0	0.3 ± 0.5		
	34527.0	$52^- \rightarrow 50^-$	2450.0	0.8 ± 0.4		

Band ID	Level energy (keV)	$I_i^\pi \rightarrow I_f^\pi$	E_γ (keV)	Intensity	R_θ	$E(\lambda)$ $M(\lambda)$
b	6126.0	$16^+ \rightarrow 14^+$	(1505.7)	3.7 ± 2.0		
	7039.0	$18^+ \rightarrow 16^+$	913.0	2.0 ± 1.2	1.40 ± 0.20	E2
	8010.5	$20^+ \rightarrow 18^+$	974.0	3.0 ± 1.5	1.40 ± 0.13	E2
		$20^+ \rightarrow 18^+$	(1503.3)	< 1.0		
	9051.3	$22^+ \rightarrow 20^+$	1040.9	4.0 ± 0.5	1.39 ± 0.10	E2
		$22^+ \rightarrow 20^+$	(1466.3)	< 0.2		
	10158.1	$24^+ \rightarrow 22^+$	1106.8	9.8 ± 3.0	1.38 ± 0.10	E2
	11331.5	$26^+ \rightarrow 24^+$	1173.4	8.9 ± 3.2	1.41 ± 0.13	E2
	12568.5	$28^+ \rightarrow 26^+$	1237.1	5.7 ± 2.3	1.39 ± 0.17	E2
	13887.2	$30^+ \rightarrow 28^+$	1318.7	4.3 ± 2.4	1.40 ± 0.19	E2
	15255.7	$32^+ \rightarrow 30^+$	1368.8	3.6 ± 0.7	1.40 ± 0.19	E2
		$32^+ \rightarrow 30^+$	1403.0	2.8 ± 1.0	1.40 ± 0.29	E2
	16727.9	$34^+ \rightarrow 32^+$	1472.2	7.7 ± 2.2	1.39 ± 0.13	E2
	18293.1	$36^+ \rightarrow 34^+$	1565.3	7.3 ± 2.7	1.40 ± 0.14	E2
	19954.6	$38^+ \rightarrow 36^+$	1661.5	7.0 ± 1.9	1.39 ± 0.16	E2
	21711.1	$40^+ \rightarrow 38^+$	1756.6	5.1 ± 1.8	1.39 ± 0.17	E2
	23563.2	$42^+ \rightarrow 40^+$	1852.1	4.4 ± 1.6	1.41 ± 0.18	E2
	25510.3	$44^+ \rightarrow 42^+$	1947.5	3.9 ± 1.5	1.38 ± 0.19	E2
	27552.1	$46^+ \rightarrow 44^+$	2041.9	2.7 ± 1.2	1.40 ± 0.23	E2
	29689.9	$48^+ \rightarrow 46^+$	2137.8	2.5 ± 1.1	1.43 ± 0.25	E2
	31920.9	$50^+ \rightarrow 48^+$	2231.0	2.1 ± 0.9	1.43 ± 0.26	E2
	34238.0	$52^+ \rightarrow 50^+$	2317.1	1.8 ± 0.6	1.43 ± 0.29	E2
	36593.3	$54^+ \rightarrow 52^+$	2360.9	1.2 ± 0.7	1.42 ± 0.32	E2
	38923.9	$56^+ \rightarrow 54^+$	2336.2	0.5 ± 0.6	1.40 ± 0.37	E2
b+	8836.2	$22^+ \rightarrow 20^+$	1250.1	1.1 ± 2.1	1.43 ± 0.23	E2
	9967.0	$24^+ \rightarrow 22^+$	1130.5	3.0 ± 1.5	1.38 ± 0.24	E2
		$24^+ \rightarrow 22^+$	1224.1	0.9 ± 1.7		E2
	11149.0	$26^+ \rightarrow 24^+$	1183.2	4.0 ± 2.5	1.40 ± 0.25	E2
	12445.4	$28^+ \rightarrow 26^+$	1297.5	9.0 ± 2.2	1.40 ± 0.26	E2
	13854.1	$30^+ \rightarrow 28^+$	1409.9	7.5 ± 1.6	1.38 ± 0.29	E2
		$30^+ \rightarrow 28^+$	1285.8	< 0.4		E2

are determined from the angular distribution of connecting transitions. If given in parenthesis, they are less certain, deduced from systematics or comparison to model predictions. In many cases, however, interwoven band structures lock mutual values.

A. Positive-parity bands

The ground state band, in ref. [2] also referred to as band 2, terminates at an 8^+ level at 2434.7 keV where it connects to band 1 which has a $\pi(h_{11/2})^2$ structure and to band 3 which has a $\nu(h_{11/2})^2$ structure [1]. The present work only extends band 3 by one transition to $I = 24$ and identifies two transitions connecting the two different $(h_{11/2})^2$ structures, bands 1 and 3, at the spin 14 and 16 levels. Bands 4 and 5, which are of vibrational nature, and lie quite high in energy above the yrast line, are only weakly populated in the $^{82}\text{Se}(^{48}\text{Ca}, \text{xn})$ reaction. Similarly, bands 6 and 7 reported in ref. [2] are not observed in the present work, probably also due to their off-yrast nature. Band 14 is observed, but not extended to higher spin in this work. It is shown in Fig. 1 with the assignments given in [2]. Band 15, not connected to the ground state levels in [2], is observed to spin and parity 27^+ in the present work, and two decay routes connecting it to the ground state are identified. One of these proceeds via levels of a structure labelled 15+ in Fig. 1, which might possibly correspond to low-lying members of a high-K band. The E2 character of the 990, 1334 and 1347 keV transitions extracted from the data gives positive parity and firm spin assignments to bands 15 and 15+. A strong E2 transition of 1319 keV populates the 27^+ level of band 15, but no further structures connected to it could be identified with certainty. Band 16 is newly observed in this work. It decays by an E2 transition into the $I^\pi = 22^+$ level of band 3 and extends by three E2 transitions

Band ID	Level energy (keV)	$I_i^\pi \rightarrow I_f^\pi$	E_γ (keV)	Intensity	R_θ	$E(\lambda)$ $M(\lambda)$
c	Y+1156.4	$(25^+) \rightarrow (23^+)$	1156.4	0.8 ± 1.2		(E2)
	Y+2380.6	$(27^+) \rightarrow (25^+)$	1224.2	2.3 ± 2.1	1.38 ± 0.17	E2
	Y+3673.3	$(29^+) \rightarrow (27^+)$	1292.7	3.3 ± 1.0	1.40 ± 0.15	E2
	Y+5043.4	$(31^+) \rightarrow (29^+)$	1370.1	5.0 ± 2.0	1.40 ± 0.13	E2
	Y+6488.3	$(33^+) \rightarrow (31^+)$	1444.9	4.7 ± 2.0	1.39 ± 0.13	E2
	Y+8014.1	$(35^+) \rightarrow (33^+)$	1526.1	4.0 ± 1.9	1.38 ± 0.14	E2
	Y+9624.0	$(37^+) \rightarrow (35^+)$	1609.6	3.1 ± 1.8	1.39 ± 0.15	E2
	Y+11320.8	$(39^+) \rightarrow (37^+)$	1696.8	1.9 ± 1.7	1.43 ± 0.15	E2
	Y+13107.5	$(41^+) \rightarrow (39^+)$	1786.7	2.0 ± 1.6	1.39 ± 0.16	E2
	Y+14984.7	$(43^+) \rightarrow (41^+)$	1877.2	1.8 ± 1.3	1.42 ± 0.16	E2
	Y+16953.2	$(45^+) \rightarrow (43^+)$	1968.5	1.3 ± 1.3	1.39 ± 0.20	E2
	Y+19004.0	$(47^+) \rightarrow (45^+)$	2050.8	1.3 ± 1.2	1.42 ± 0.25	E2
	Y+21097.0	$(49^+) \rightarrow (47^+)$	2093.0	1.0 ± 1.0	1.44 ± 0.32	E2
	Y+23226.4	$(51^+) \rightarrow (49^+)$	2129.4	0.8 ± 1.0	1.44 ± 0.32	E2
	Y+25413.8	$(53^+) \rightarrow (51^+)$	2187.4	0.6 ± 1.4		(E2)
	Y+27673.5	$(55^+) \rightarrow (53^+)$	2259.7	0.4 ± 1.0		(E2)
	Y+30018.0	$(57^+) \rightarrow (55^+)$	2344.5	0.3 ± 0.6		(E2)
	Y+(32345.7)	$(59^+) \rightarrow (57^+)$	(2327.7)	<0.1		(E2)
d	X+1034.7	$(25^-) \rightarrow (23^-)$	1034.7	6.2 ± 2.1	1.39 ± 0.17	E2
	X+2184.2	$(27^-) \rightarrow (25^-)$	1149.5	7.3 ± 3.9	1.42 ± 0.16	E2
	X+3453.0	$(29^-) \rightarrow (27^-)$	1268.8	6.3 ± 2.9	1.37 ± 0.16	E2
	X+4839.6	$(31^-) \rightarrow (29^-)$	1386.6	4.8 ± 1.6	1.39 ± 0.17	E2
	X+6341.8	$(33^-) \rightarrow (31^-)$	1502.2	4.4 ± 1.5	1.38 ± 0.18	E2
	X+7944.7	$(35^-) \rightarrow (33^-)$	1602.9	4.1 ± 1.3	1.43 ± 0.20	E2
	X+9654.2	$(37^-) \rightarrow (35^-)$	1709.5	1.2 ± 1.1	1.41 ± 0.22	E2
	X+11477.5	$(39^-) \rightarrow (37^-)$	1823.3	1.1 ± 1.1	1.43 ± 0.21	E2
	X+13417.1	$(41^-) \rightarrow (39^-)$	1939.6	1.0 ± 1.3	1.42 ± 0.23	E2
	X+15466.8	$(43^-) \rightarrow (41^-)$	2049.8	1.0 ± 1.3	1.44 ± 0.32	E2
	X+17616.9	$(45^-) \rightarrow (43^-)$	2150.0	0.9 ± 1.0	1.41 ± 0.35	E2
	X+19853.7	$(47^-) \rightarrow (45^-)$	2236.8	0.6 ± 0.8	1.45 ± 0.44	E2
	X+22174.5	$(49^-) \rightarrow (47^-)$	2320.8	0.3 ± 0.5	1.40 ± 0.25	E2
	(X+24598.9)	$(51^-) \rightarrow (49^-)$	(2424.4)	<0.1		(E2)

TABLE II: Level energies, spin and parity assignments, γ -ray energies, relative intensities, angular distribution ratios R_θ (see section III), and assignment of multipole order of transitions in bands **a** - **d**. All transitions are newly observed in this work. The intensities are measured relative to the 388.3 keV $2^+ \rightarrow 0^+$ groundstate transition. Closely lying and weak transitions are fitted separately, while the intensities of the stronger lines are fitted with routines of the Radware program package [11]. Bands **a** and **b** are connected. Bands **c** and **d** are not connected to lower lying structures by known transitions. Level energies are indicated by the sum of Y or X and the transition energies of the two bands, respectively.

to an $I^\pi = 30^+$ state, but no further transitions to higher energies or any signature partner to band 16 could be found.

The newly identified band **b** connects to the $\nu(h_{11/2})^2$ structure of band 3 at the $I = 14$ and 16 levels, as shown in Fig. 1, and extends to $I = 56$ at an excitation energy of 38.9 MeV as indicated in Fig. 2. The double-gated spectrum on clean transitions beyond $I = 30$, presented in Fig. 3, documents the coincidence relationships of band **b** and its forking structure **b**⁺. The 1250 keV quadrupole transition determines $I = 22$ for the bottom level of band **b**⁺, and the 1403 keV and 1286 keV E2 transitions feeding and depopulating the $I = 30^+$ level of band **b**⁺ firmly connect the two bands. Both bands have parity and signature $(\pi, \alpha) = (+, 0)$ and they interact at $I^\pi = 30^+$.

Although not connected to the low-lying bands by firm evidence, the placement of band **c** shown in Figs. 1 and 2 is the most probable considering transition energies and intensities in the band. The suggested assignment as the $(+, 1)$ partner of band **b** agrees with this placement and will be discussed further in section IV. The decay of band **c** into lower lying structures involve the 29^+ level feeding band 15 mentioned above.

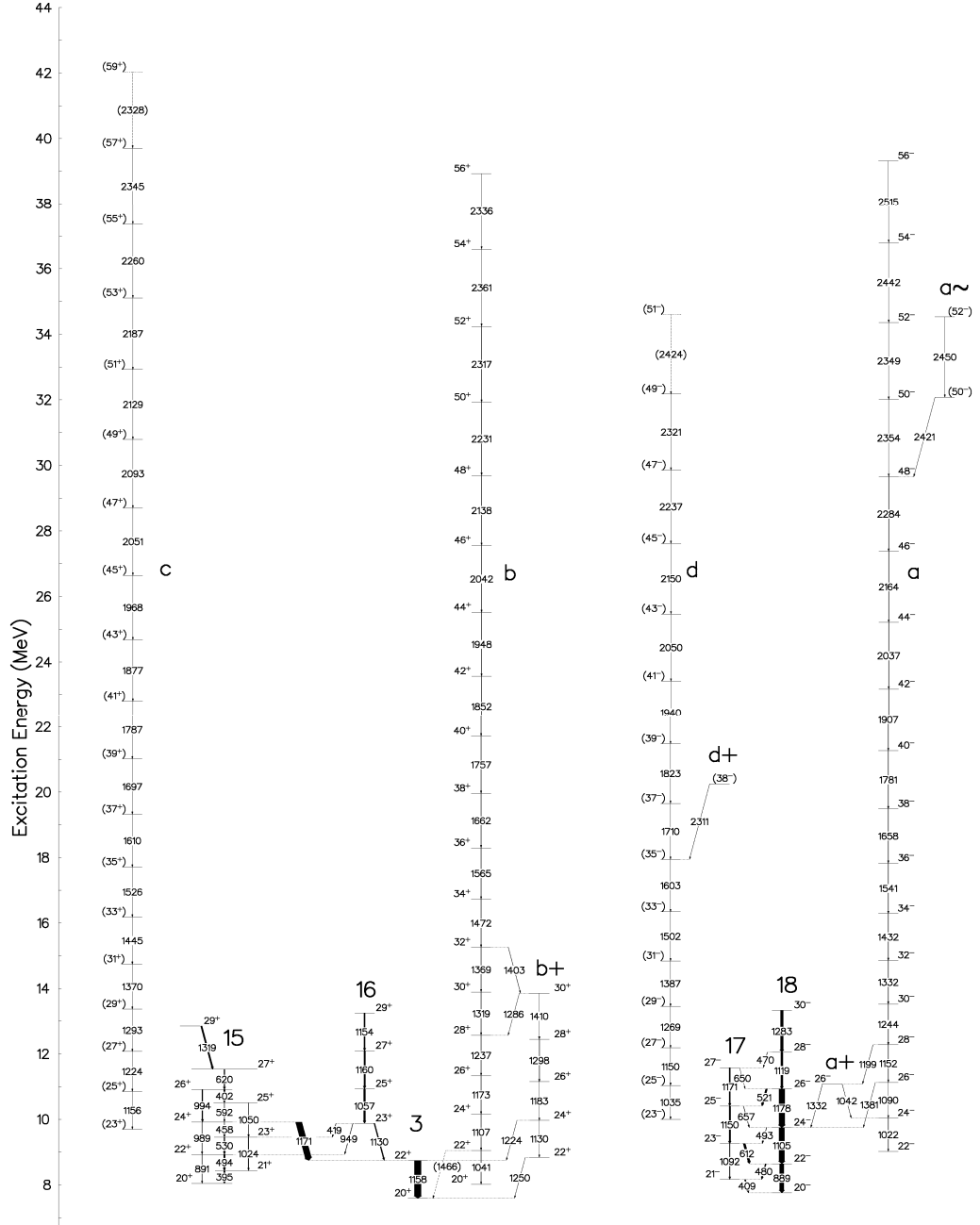


FIG. 2: Partial, high-spin level scheme of ^{126}Xe . The newly identified collective structures are labelled **a**, **b**, **c** and **d** while previously reported levels [2] are labelled 3 and 15. New levels and transitions have been added to band 15, whereas bands 16, 17 and 18 are new.

B. Negative-parity bands

Altogether ten different negative-parity bands are observed in the present work, two of them extending to spins beyond 50. The lowest lying of the negative-parity bands are band 8 and its most probable signature partner, band 9. In ref. [2] evidence is given for an $I^\pi = 3^-$ bandhead. In the present work, however, most of the in-band intensity is drained at $I^\pi = 7^-$ by a 1245 keV transition to the 8^+ level of the ground state band. Only a weak

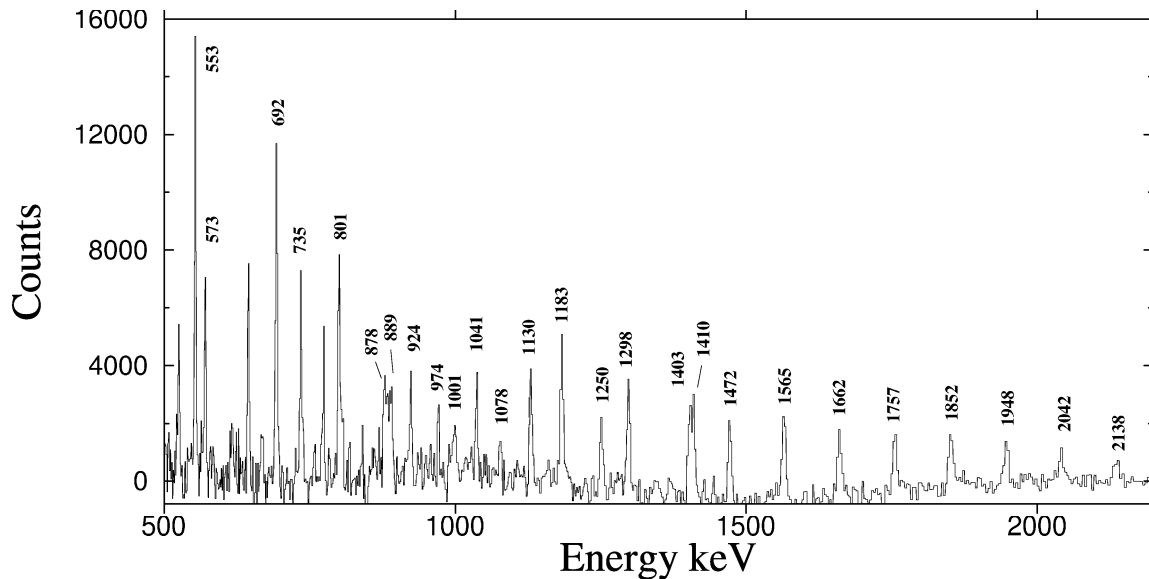


FIG. 3: Double-gated spectrum of band **b** illustrating the decay into band 3 and eventually the ground state band. The spectrum was created with two gate-lists containing transitions at [1757, 1662, 1565, 1472] and [1403, 1410, 1298, 1183] keV, respectively. The strong unmarked γ rays below 800 keV are known transitions in the neighboring nucleus ^{125}Xe . The reduced intensity of the peaks in the 1100 - 1800 keV region is due to the eight gates imposed in this energy interval.

decay is seen to the 5^- state, but no connection to the 3^- level is identified. Similarly, the low-lying levels of band 9 reported in ref. [2] are not observed. The 8^- state at 3196.6 keV decays into the $I^\pi = 7^-$ level of band 8 and with a very weak branch to the 8^+ state of the ground band. The failure to observe the low-lying transitions in bands 8 and 9 can be explained by a different side-feeding to the low-lying states of these bands in the $^{82}\text{Se}(^{48}\text{Ca}, \text{xn})$ reaction.

Bands 10 and 11 are presumably also signature partners with a structure very similar to bands 8 and 9. A 802 keV transition from band 9 into the $I = 12$ level of band 11 and weak transitions from band 11 into band 10 at the spin 8 and 6 levels supports this suggestion. The spin and parity assignments of band 10 are firm and the $(-,0)$ assignment of band 11 is, therefore, the most probable. All four structures are populated by the two newly observed bands 17 and 18 which most likely are higher-seniority quasiparticle bands and which we identify as signature partners with $(\pi, \alpha) = (-,1)$ and $(-,0)$, respectively. A fourth pair of negative parity signature partners is bands 12 and 13. The 955 keV E1 transition to the 6^+ state of the ground band confirms the 7^- assignment of the 2589.3 keV level of band 13. A 750 keV transition connects the 27^- level of band 13 to the 26^- state of band 18 and provides a further check on the assignments.

Two of the newly observed long bands, extending beyond spin 50, presumably have negative parity and are shown as bands **a** and **d** in Fig. 2. Their features and assignments will be discussed in section IV.

The connection of band **a** to the lower-lying structures is illustrated by the spectrum presented in Fig. 4. The band connects to band 18, which has a parity and signature assignment of $(-,0)$, through an isolated level at 11 MeV with $I^\pi = 26^-$ by a 1332 keV E2 transition. The 26^- level decays also back into band **a**, presumably due to mixing of the two 26^- states. Parity and signature of the two bands are, therefore, the same. The lowest state of band **a** has spin 22^- at 9 MeV and the band extends by 17 consecutive E2 transitions to $I^\pi = 56^-$ at 39 MeV.

The placement of band **a** shown in Fig. 2 could in principle be lifted by two units of spin. The appearance of the 1178 keV transition, visible in the spectrum shown in Fig. 4., could indicate that the 1332 keV transition from the $I^\pi = 26^-$ level labelled **a**⁺ could populate band 18 at its $I = 26^-$ level at 10927.3 keV and not the $I^\pi = 24^-$ state which is 1178 keV lower in energy. Since there are transitions of similar energy elsewhere in the ^{126}Xe level scheme and in the neighboring isotopes, the placement based on triple and quadruple coincidences alone has some uncertainty. We will come back to this question in the discussion of section IV, using arguments from derived quantities.

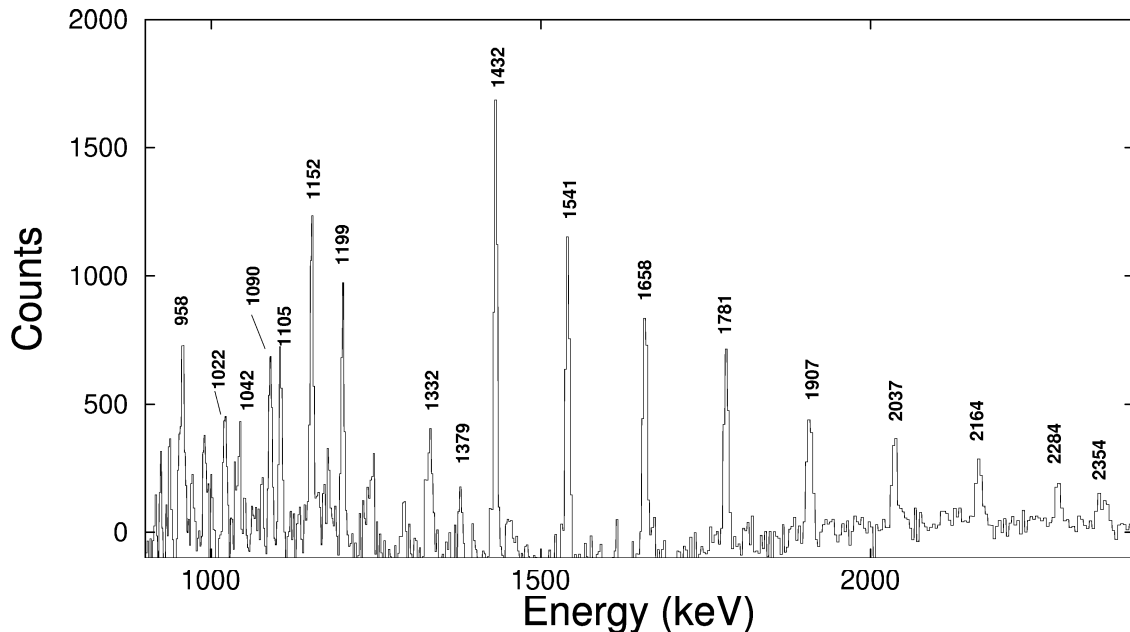


FIG. 4: Double-gated spectrum of band **a** illustrating the decay into bands 17 and 18 via the intermediate \mathbf{a}^+ level. The 1332 keV transition is in self coincidence. The appearance of a weak 1178 keV peak might suggest a placement of level \mathbf{a}^+ two spin units higher than shown, and band **a** lifted 1178 keV in energy, see text.

C. Population of the highest-spin states

The population of band **a** is the highest among the bands extending beyond spin $I = 50$ and the intensity of the $30 \rightarrow 28$, 1244 keV transition of this band is 1.3% of the ground state transition. The relative intensities of bands **a** to **d** have been estimated from spectra created with a sum of six double gates in each of the four bands placed on either side of a transition of about 1600 keV. Relative to band **a**, the strengths of bands **b**, **c** and **d** are 0.9, 0.6 and 0.4, respectively, in the spin range 32 - 44.

As shown in Figs. 1 and 2, the bands numbered 15 - 18 are not identified to spins higher than about $30 \hbar$ in the present work. This does not mean that there are no coincident transitions preceeding those drawn in the figures. One example is the precursors of the assigned $30^+ \rightarrow 28^+$, 1283 keV transition of band 18. Among these precursors we find a relatively strong γ ray of 2545 keV and a number of weaker ones in the energy range from 1500 to 1800 keV. None of these feeding transitions could be placed into a regular band structure and one might surmise that band 18 as well as some of the other bands terminate at about spin 30.

D. Transition quadrupole moment of band a

The recoiling Xe ions require about 100 fs to penetrate the $500 \mu\text{g}/\text{cm}^2$ Se target, which implies that γ rays from highly excited, rapidly rotating deformed nuclei will be emitted during their passage through the target. Even though this target is thin, the velocity v/c of the recoiling nuclei varies by about 6 % from one end to the other and this variation is sufficient for measurements of fractional Doppler shifts, F_τ , for the fastest transitions, as demonstrated in refs. [12, 13].

An average transition quadrupole moment Q_t for the strongest populated band **a** has been deduced from the fractional shifts which were determined from the velocity calculated from the kinematics of the reaction and from the experimental recoil velocities. A simple rotational model and tabulated stopping powers [14] were used for a fit to the F_τ values

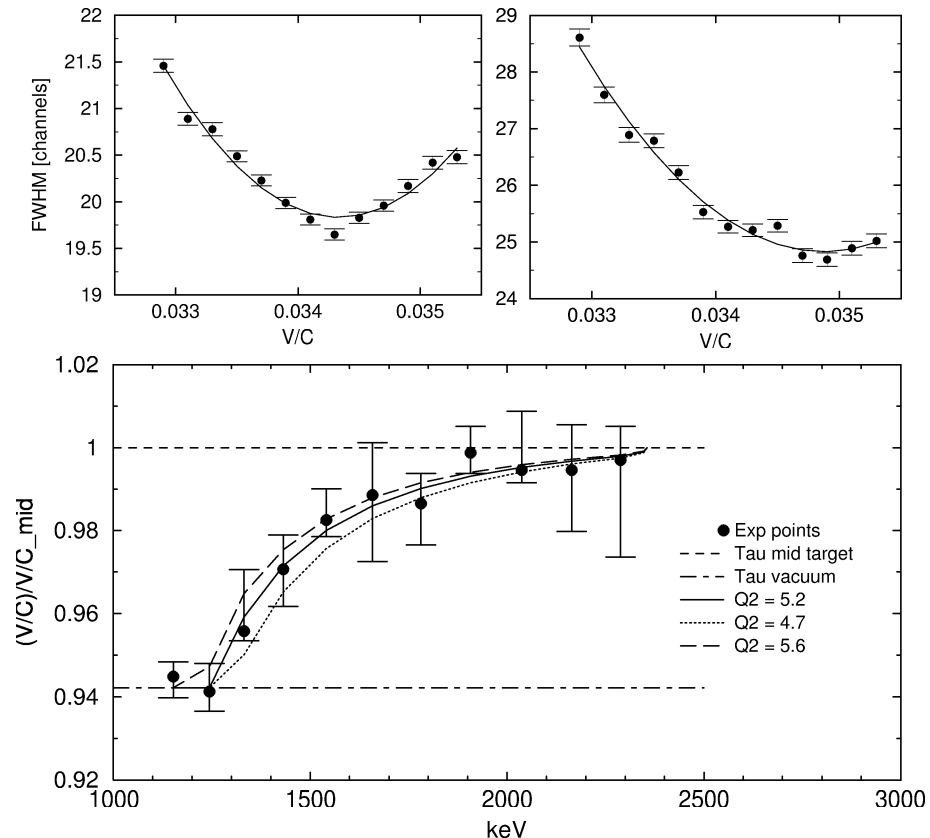


FIG. 5: Peak width analysis of the 1540 keV $36^- \rightarrow 34^-$ and the 1907 keV $42^- \rightarrow 40^-$ transition in band **a** shown in the left and the right upper panels, respectively. The lower panel presents the fractional Doppler shifts for 11 transitions of band **a** based on the minimum FWHM as a function of v/c . Curves calculated for three different values of the transition quadrupole moment are compared and the value $Q_t = 5.2$ b is adopted.

with the quadrupole moment as a free parameter. Estimates of the velocity which the ^{126}Xe -recoil had at the emission of a given transition in band **a** were determined from gated spectra produced at 13 different values of v/c . The FWHM for the peaks were obtained from fits using Radware programs [11]. Fig. 5, upper left panel, shows a minimum at $v/c = 0.0344$ for the 1540 keV $I = 36 \rightarrow 34$ transition. The upper right panel of Fig. 5 shows a minimum at a larger v/c for the 1907 keV $I = 42 \rightarrow 40$ transition, emitted three steps earlier in the cascade. In this way the minimum FWHM was determined for 11 transitions and the corresponding v/c values in the energy range from 1100 to 2300 keV were normalised to the v/c value at the middle of the target as shown in the lower panel of Fig. 5. The best fit to the experimental values is obtained for $Q_t = 5.2^{+0.4}_{-0.5}$ b. Curves for $Q_t = 4.7$ and 5.6 b are also shown, indicating the sensitivity of the method. The adopted value corresponds to an axis ratio of ~ 1.3 for an axially symmetric deformed Xe nucleus.

IV. DISCUSSION OF THE LONG HIGH-SPIN BANDS

The four long collective bands, **a**, **b**, **c** and **d**, newly identified in the present work, extend into the spin region near $I = 60$. At this limit, even the structures close to yrast have intensities below the detection sensitivity of the Gammasphere array for discrete-line spectroscopy in ^{126}Xe . In the following we will discuss the properties of these four bands, relating them to the transition quadrupole moments, their position in the energy-spin plane, the dynamic moment of inertia, the evolution of alignment and theoretical calculations with the UC code [5]. As the present data do not add decisive new information to the low-spin part of the level scheme, we will not repeat comments on the earlier configuration assignments [1, 2].

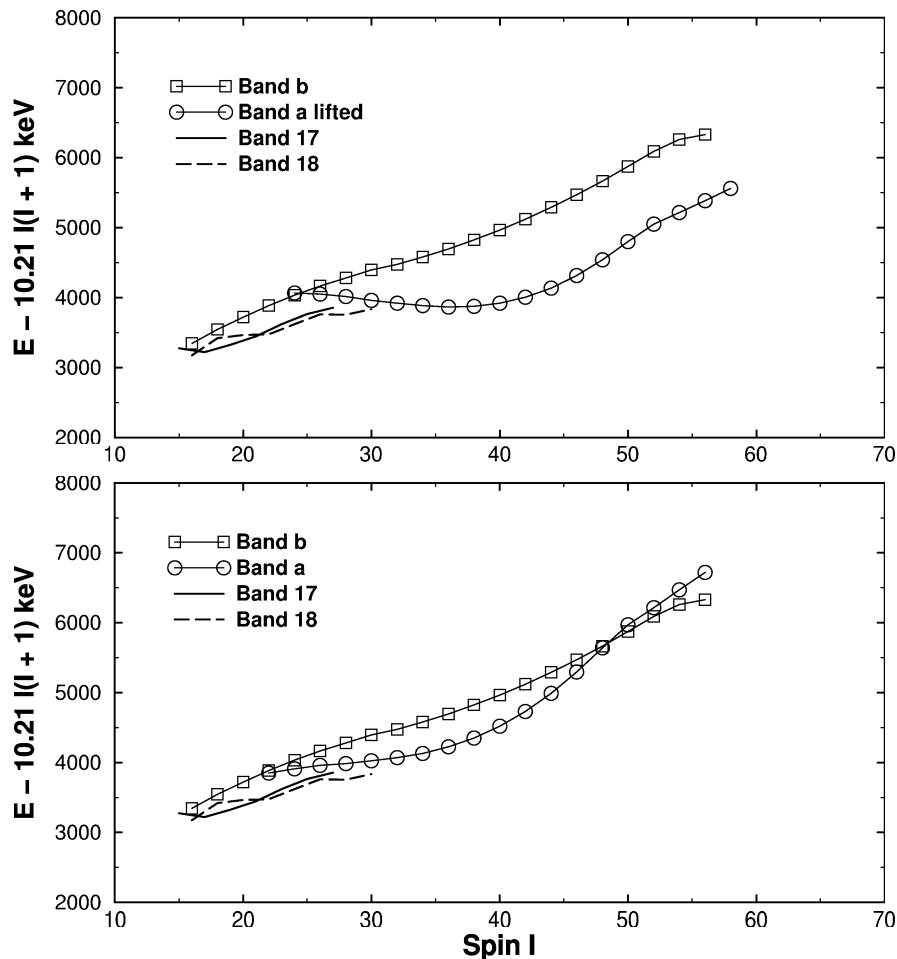


FIG. 6: Level energies of bands **a**, **b**, 17 and 18, with the energy of a rotating rigid core subtracted, are shown as a function of spin for two placements of band **a**. The lower panel shows band **a** for the adopted placement shown in Fig. 1 and 2, while the upper panel shows the band lifted by two units of spin and 1178 keV in energy.

First, we want to make some general comments on the level scheme related to the long bands. There are missing links in the level structure shown in Figs. 1 and 2; only band **b** is firmly linked to the low-lying structures. The strongest populated band, band **a**, is linked as shown in Fig. 1 with very high certainty, but due to the many energy degeneracies of the γ -ray energies, as mentioned in section III B, this band could possibly be lifted up by two spin units and 1178 keV in energy. Fig. 6 shows the level energies of bands **a** and **b**, with a rigid rotor reference subtracted, as a function of spin. For band **a** the two placements discussed here are shown. In the lower panel, the band is placed as shown in Fig. 1, while the upper panel presents the band lifted by two spin units and 1178 keV in excitation energy. The higher spin and level energy lowers band **a** in the energy-spin plane and would result in a much stronger population relative to band **b** than the 10 % difference we observe, see section III C. We find from Table II that band **a** receives 37 units of intensity in the spin range 32 - 44, while band **b** receives 35 units. This is, within uncertainties, in agreement with the 10 % difference in population extracted by the multiple-gating technique described in section III C. In the spin range of 48 to 54, however, the intensity ratio between bands **a** and **b** is inverted. Here the population intensity of band **b** is 5.6 units compared to 3.2 units for band **a** which is in agreement with band **b** being closer to yrast than band **a** in this spin range. On the basis of these experimental intensities and the evolution of the two bands in the energy-spin plane, see Fig. 6, we conclude that the lower panel is the only one agreeing with the experiment and that the placement of band **a**, therefore, is most likely as proposed in Fig. 1. Accordingly, no parentheses on spin and parity are used for band **a**. Band **a** becomes yrast above $I \sim 30$, where bands 17 and 18 appear to terminate as regular rotational structures.

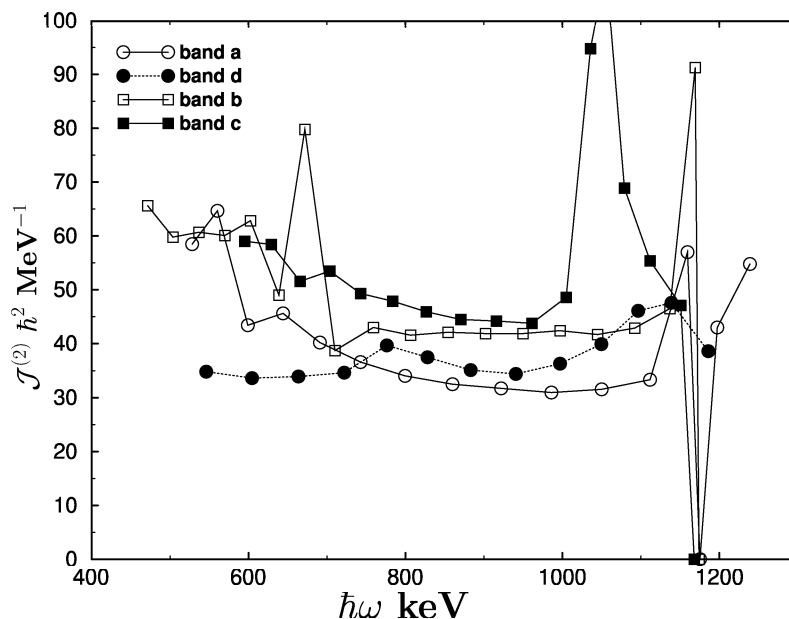


FIG. 7: Dynamic moments of inertia for the four long bands as a function of rotational frequency. Band crossings are seen at 1050 and at 1170 keV while the spike at 675 keV is caused by an interaction between the 30^+ states in bands **b** and **b** $^+$.

The dynamic moments of inertia $\mathcal{J}^{(2)}$, presented in Fig. 7, do not depend on assigned spin values while the spin alignments, shown in Fig. 8, do. The dynamic moments of inertia show a grouping of the four long bands in pairs of **a**, **d** and **b**, **c**, which is consistent with the decay of the pair **a**, **d** to the lower-lying negative-parity structures and of the pair **b**, **c** to the positive-parity states. Another feature of the evolution of $\mathcal{J}^{(2)}$ is a relative constancy over a frequency range of about 500 keV. The irregularity at $\hbar\omega \sim 700$ keV for band **b** is caused by its interaction with band **b** $^+$ at $I = 30$ which can be removed by a shift of ~ -15 and $+15$ keV of the 30^+ levels of bands **b** and **b** $^+$, respectively. When comparing average values of $\mathcal{J}^{(2)}$ in the range $\hbar\omega \sim 750 - 1100$ keV, we observe a difference of $\sim 10 \hbar^2/\text{MeV}$ between the two pairs which might be interpreted as a difference in deformation, bands **b** and **c** being the more deformed ones. The average values of $\mathcal{J}^{(2)} = 35 \hbar^2/\text{MeV}$ and $45 \hbar^2/\text{MeV}$, respectively, are far from the value of $56.4 \hbar^2/\text{MeV}$, which is the calculated moment of inertia for a rigid prolate nucleus with an axis ratio of 1/1.3, corresponding to the value of Q_t determined for band **a** if assuming axial symmetry, see section III D. This discrepancy might indicate that the system is not rigid, even at the highest spins observed in band **a**. However, as discussed below, the UC calculations reproduce both the quadrupole moment and the moments of inertia rather well. We note that the dynamic moments of inertia indicate crossings in all bands near $\hbar\omega = 1170$ keV and for band **c** another crossing at about 1050 keV.

The alignment of the long bands shows the simultaneous crossing of bands **a**, **b** and **c** at about 1170 keV, see Fig. 8. Band **d** does not indicate a crossing in this frequency region, but the trend of the alignment considering the last four transitions of this band could be explained by an unobserved forking transition. The dwindling intensity in band **d** at the highest spins and the observed forking of band **a** into **a** \sim at $\hbar\omega \sim 1200$ keV support this suggestion. The additional crossing in band **c** at $\hbar\omega \sim 1050$ keV is clearly identified in Fig. 8.

We shall compare three of the features identified in Figs. 7 and 8 to results of UC calculations in some detail. One is the pairwise appearance of the four long bands, the other is the constancy of the $\mathcal{J}^{(2)}$ value over a frequency range of about 500 keV and the third is the common upbend at a frequency of about 1170 keV. The experimental estimate of Q_t discussed in section III D for band **a** compares well with a potential energy minimum obtained in the UC calculations [5] at $(\epsilon, \gamma) \sim (0.35, 5^\circ)$ and $\epsilon_4 \sim 0$. This minimum in the potential energy surface emerges at $I \sim 20$ and is stable over a long spin range, in particular the lowest calculated quasiparticle configurations which correspond to the parity and signature combinations (π, α) possible for the four long bands. The agreement between the measured $Q_t = 5.2$ b and the values of Q_2 calculated within this minimum is clear from Fig. 9. (The UC code calculates the (static) electrical quadrupole moment which may be related to the measured transition quadrupole

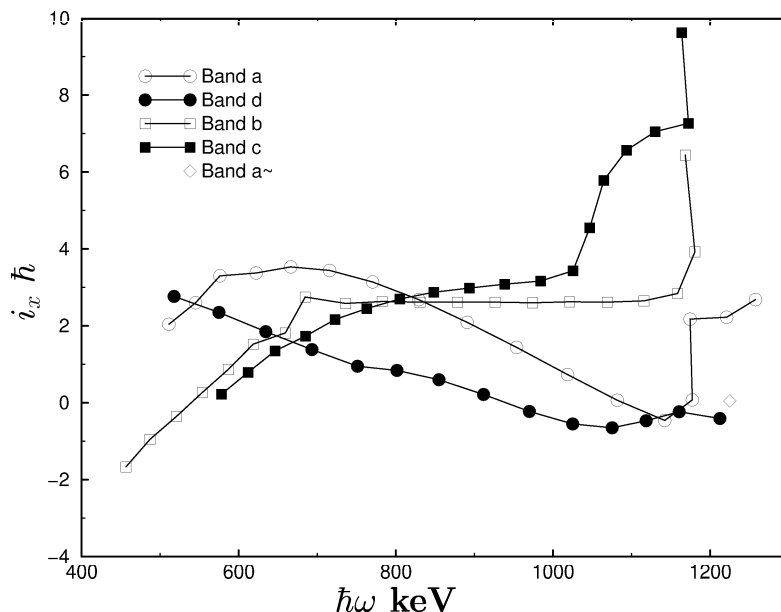
Band	Parity, signature (π, α)	protons orbitals, signature	neutrons orbitals, signature
a	(-,0)	$g_{7/2}^2 \otimes h_{11/2}^2, 0$	$i_{13/2} \otimes h_{11/2}, 0$
d	(-,1)	$g_{7/2}^2 \otimes h_{11/2}^2, 0$	$i_{13/2} \otimes h_{11/2}, 1$
b	(+,0)	$g_{7/2} \otimes h_{11/2}, 0$	$i_{13/2} \otimes h_{11/2}, 0$
c	(+,1)	$g_{7/2} \otimes h_{11/2}, 0$	$i_{13/2} \otimes h_{11/2}, 1$

TABLE III: Proton and neutron orbitals excited in bands **a**, **b**, **c** and **d** below ~ 0.7 MeV.

moment within a regular rotational band with a stable shape, $Q_2 \equiv Q_t$). The further discussion of the four bands will, therefore, relate to the structural features at this minimum.

The proton orbitals available close to the Fermi level are $g_{7/2}$ and $i_{13/2}$ with positive parity and $h_{11/2}$ with negative parity. For the neutrons, the $i_{13/2}$ orbitals with positive parity and the $h_{9/2}$, $h_{11/2}$ and $j_{15/2}$ orbitals with negative parity are available. We note that the latter neutron orbital as well as the $i_{13/2}$ proton orbital have large negative slopes of the energy as a function of frequency, $d(e)/d(\omega)$, and are, therefore, most probably active in the observed band crossings at high frequencies. The lowest structures with relevant spins and frequencies which have parity and signature (-,0) and (-,1) as bands **a** and **d** or (+,0) and (+,1) as bands **b** and **c**, have two to four quasiparticles excited in both the proton and the neutron systems. The lowest solutions involve $g_{7/2}$ and $h_{11/2}$ protons coupled to $i_{13/2}$ and $h_{11/2}$ neutrons, as shown in Table III.

An alternative structure for bands **b** and **c** is obtained by a simultaneous change of the signature quantum numbers of the occupied $h_{11/2}$ neutron and $g_{7/2}$ proton orbitals, which is not expected to change the band properties

FIG. 8: Alignment of bands **a**, **b**, **c**, **d**, and **a~** with Harris parameters $\mathcal{J}_0 = 42 \hbar^2/\text{MeV}$ and $\mathcal{J}_1 = 0$.

substantially. Both orbitals have no or a very small signature splitting in the relevant deformation and frequency region. The difference between the two pairs is, thus, to be traced to the excited quasiprotons, since the neutron excitations are pairwise identical. The positive-parity bands **b** and **c** have the $h_{11/2}^2$ alignment blocked, which may explain the difference in the alignment behaviour of the two pairs of bands, which is also observed experimentally.

Structural changes resulting in an increase of the alignment might be expected for both pairs in at least two situations. Firstly, at frequencies around 0.85 - 0.9 MeV where the $i_{13/2}$ proton competes and crosses the $g_{7/2}$ proton with $\alpha = +1/2$ and, secondly, at frequencies around 1.2 MeV where the $j_{15/2}$ neutron competes with the $h_{11/2}$ neutron. Softer alignments are expected for the higher-frequency $i_{13/2}$ neutron crossing and are, therefore, not considered for causing the dramatic upbends experimentally observed in bands **a**, **b** and **c**. We note that the location of the $i_{13/2}$ proton orbital is strongly dependent on deviations from axial symmetry of the nuclear shape, and that this might argue against the first conjecture mentioned above. For the common alignment gain observed at $\hbar\omega \sim 1.17$ MeV we, therefore, suggest that the $j_{15/2}$ neutron has to be involved. For such multiquasiparticle bands it may be expected that pairing correlations are strongly reduced.

It is a striking feature of the UC calculations that our suggestion for bands **a** and **d** as signature partners with negative parity and bands **b** and **c** with positive parity is corroborated very nicely. Fig. 9 shows the UC predictions for the quadrupole moment, the quadrupole deformation and the gamma deformation in the lower, middle and top panels, respectively, as a function of spin. The pairwise features are very clear and the constancy of the calculated Q_2 , ϵ and γ deformations over an interval of about 30 units of spin in the range where the bands are observed is convincing and gives confidence in the (π, α) assignments to the bands. Furthermore, the UC code provides coordinates in the energy-spin plane which allow a comparison to experimental data in graphs (not shown) corresponding to Fig. 6. The calculated bands **a** and **b** are, in this representation, separated by ~ 500 keV from $I \sim 30$ to 40, and they cross at $I \sim 48$ as in the experiment, see Fig. 6, lower panel. The signature partners, bands **d** and **c**, exhibit the same trend as bands **a** and **b**. All three calculated quantities displayed in Fig. 9 start to deviate from their regular trends at about spin 45, a feature which has its basis in the relevant potential energy surfaces. The stable minimum at $\epsilon \sim 0.35$ gradually disappears for bands **a** and **d**, while it moves to larger γ values. The calculated values of Q_2 shown in Fig. 9 indicate a larger deformation for bands **b** and **c** than for the negative-parity pair. However, this difference is entirely based on a difference in non-axial symmetry which would barely be reflected in a larger moment of inertia. For a more direct comparison with data, we have extracted the dynamic moment of inertia $\mathcal{J}^{(2)}$, equivalent to $dI/d\omega$, with the UC code for the two pairs. In the frequency region $\hbar\omega \sim 0.5 - 0.6$ MeV, the negative-parity pair has an average $\mathcal{J}^{(2)}$ of $\sim 30 \hbar^2/\text{MeV}$ while the $\mathcal{J}^{(2)}$ of the positive-parity pair is $\sim 43 \hbar^2/\text{MeV}$. In the frequency range about 200 keV higher, the pairwise splitting persists with $\sim 32 \hbar^2/\text{MeV}$ and $\sim 38 \hbar^2/\text{MeV}$ for the negative- and the positive-parity pair, respectively. The agreement with the experimental data in Fig. 7 is very satisfactory, also with regard to the decreasing trend of the absolute values.

Fig. 10 displays the experimental yrast levels together with a calculated yrast line, neutron separation energy, fission barrier and, at the highest spins, an yrast line expected for hyperdeformed (HD) states in ^{126}Xe , see figure caption for details. In neither of the spectra based on the Xe1 data set from Euroball nor the Xe2 data set from Gammasphere, do we find discrete transitions which link the bands shown in Fig. 1 and 2 directly to discrete band structures in a HD minimum. Fig. 10 demonstrates that the gap in excitation energy and angular momentum between the top of bands **a** and **b** and the calculated HD yrast line is only about 3.5 MeV and ~ 5 units of spin, respectively, corresponding to 2 - 3 transitions of E2 character. However, a filtering of high-fold events [15] with the characteristics of bands **a**, **b**, **c** and **d** reveals a ridge structure in the unresolved quasicontinuum spectra with a distance between the ridges corresponding to an energy difference between consecutive rotational transitions of $\Delta E_\gamma \sim 48$ keV. The energy difference relates to the moment of inertia as

$$\Delta E_\gamma = \frac{4\hbar^2}{\mathcal{J}^{(2)}}$$

and corresponds to a value of $\mathcal{J}^{(2)} = 83 \hbar^2/\text{MeV}$. Such a large moment of inertia is evidence for a strongly deformed rotor. However, it is smaller than the $\sim 100 \hbar^2/\text{MeV}$ expected for hyperdeformation in ^{126}Xe and rather suggests that the ridges originate from superdeformed states [16]. A detailed analysis of the ridges by a fluctuation technique [17] reveals that they represent about 10 bands with a γ -ray multiplicity in the range from 18 to 26.

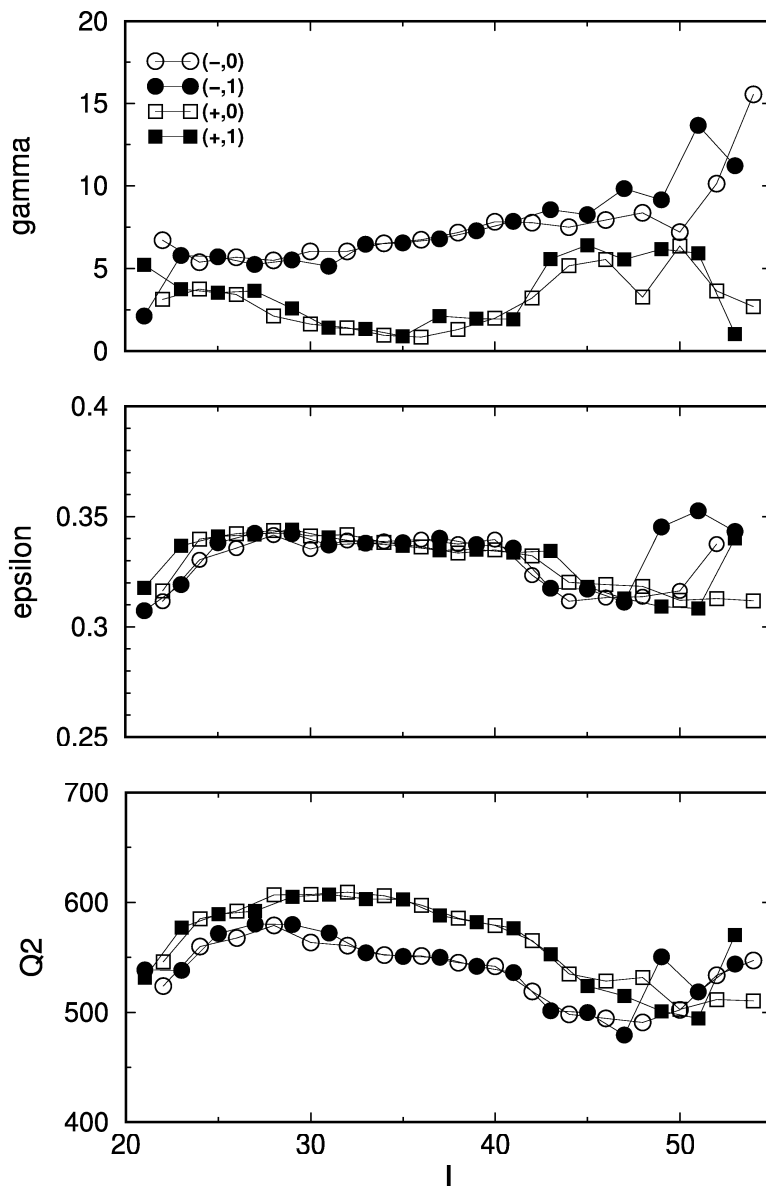


FIG. 9: Results of UC calculations for the quadrupole moment Q_2 in barns, the quadrupole deformation parameter ϵ and the gamma deformation in degrees, shown in the lower, middle and upper panels, respectively. The structures with $(\pi, \alpha) = (-, 0)$, $(-, 1)$, $(+, 0)$ and $(+, 1)$ correspond to the experimentally observed bands **a**, **d**, **b** and **c**, respectively.

V. CONCLUSIONS

The nucleus ^{126}Xe has been populated to very high spins in two experiments where the most powerful Ge-detector arrays worldwide, Euroball and Gammasphere, have been used. Calculated values for the angular momentum inputs, taking target deformations into account, gives a maximum of $90 \hbar$. This should be sufficient to populate HD structures and to study their decay towards the ground state. In spite of a number of ancillary detectors, high statistical accuracy and good energy resolution of the Ge-detector arrays, no discrete-line spectra originating from rotating HD nuclei could be identified.

Instead, the results have provided new, detailed structure information in an energy range up to about 42 MeV of excitation and 59 units of spin in ^{126}Xe . The most striking feature of these structures is the presence of four regular bands which span a spin range of almost $40 \hbar$. The structure of these bands has been compared to cranked shell model

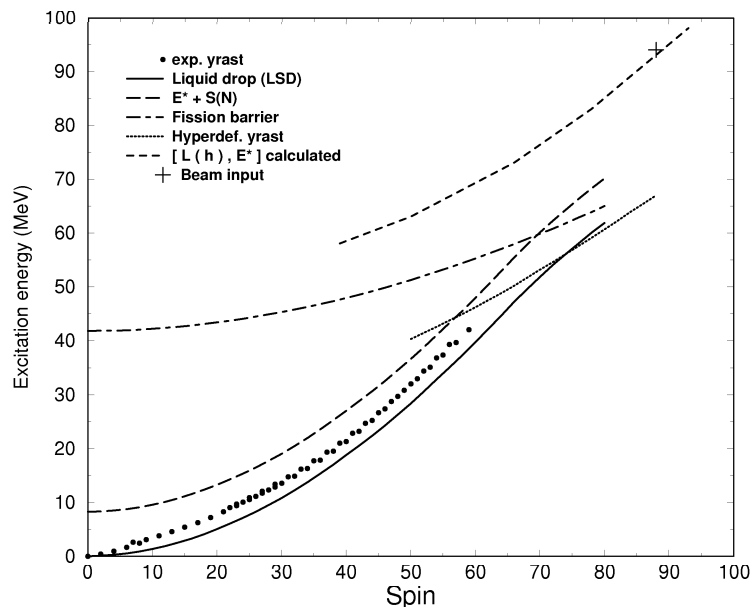


FIG. 10: Yrast diagram for ^{126}Xe . The experimentally measured yrast level energies are plotted as filled dots. The calculated yrast line based on the LSD model [4] is shown as a solid line. The long dashed curve shows the sum of the calculated yrast energy and the neutron separation energy $S(N)$. The fission barrier [4] is shown as a dashed - dot line. The yrast line corresponding to a hyperdeformed band with a moment of inertia $100 \hbar^2/\text{MeV}$ is drawn with small dots. The calculated maximum angular momentum and excitation energy input from the reaction is indicated by a plus sign.

calculations with the UC code [5] and good correspondence between experiment and theory has been demonstrated. The analysis of peak shapes in the strongest populated band has given a value for the transition quadrupole moment which agrees well with the one calculated by the UC code for states in a deformed potential-energy minimum. The properties of four of the calculated band structures reproduce parities, signatures, moments of inertia and crossing frequencies of the four experimentally observed bands very well. The band structures extend to within $\sim 2 - 3$ transitions from a crossing with the predicted HD yrast line. A ridge analysis of the unresolved quasicontinuum spectra from the present set of data indicates that the four long bands are preceded by quasicontinuum bands located in a superdeformed minimum.

VI. ACKNOWLEDGEMENTS

The authors thank the staff of the former IReS institute for the operation of the VIVITRON and the Euroball array under contract EUROVIV HPRI-CT-1999-00078. The authors also thank the ANL operations staff at Gammasphere and are indebted to J.P. Greene for his help in target preparation. G. Sletten is grateful to the GANIL management for providing excellent working conditions during the writing phase of this work. This research has been supported by the Danish FNU council for the natural sciences, by the German BMBF under contract no. 06 BN 109, by the Polish Ministry of Science and Higher Education, under grant P03B 030 30 and by the U.S. Department of Energy, Office of Nuclear Physics under contracts DE-AC02-06CH11357 (ANL) and DE-AC03-76SF00098 (LBNL).

-
- [1] A. Granderath, P.F. Mantica, R. Bengtsson, R. Wyss, P. von Brentano, A. Gelberg and F. Seiffert, Nucl. Phys. **A597**, (1996), 427-471.
 - [2] F. Seiffert, W. Lieberz, A. Dewald, S. Freund, A. Gelberg, A. Granderath, D. Lieberz, R. Wirowski and P. von Brentano, Nucl. Phys. **A554**, (1993), 287-321.

- [3] S. Cohen, F. Plasil and W.J. Swiatecki, *Ann. Phys. (N.Y.)* (1974) 557, (and W.J.S. private com.)
- [4] K. Pomorski and J. Dudek, *Phys. Rev* **C67**, (2003), 044316; N. Schunck, J. Dudek and B. Herskind, *Phys. Scr. T125* (2006) 218, and N. Schunck, J. Dudek and B. Herskind, to be published *PRC* (2007).
- [5] R. Bengtsson, <http://www.matfys.lth.se/~ragnar/ultimate.html>.
- [6] B. Herskind, G. Benzoni, J.N. Wilson, T. Døssing, G.B. Hagemann, G. Sletten, C. Rønn Hansen, D.R. Jensen, A. Bracco, F. Camera, et al. *Acta. Phys. Pol. B34*, (2003) 2467-2480.
- [7] H. Hübel, *Acta Physica Polonica*, B36, (2005) 1015.
- [8] <http://eballwww.in2p3.fr/EB/>
- [9] <http://www-gam.lbl.gov>
- [10] J.P. Green, *Application of Accelerators in Research and Industry*, ed. J.L. Duggan and I.L. Morgan, AIP (1999), 929 - 931.
- [11] D. Radford, <http://radware.phy.ornl.gov/>
- [12] B. Cederwall, I.Y. Lee, S. Asztalos, M.J. Brinkman, J.A. Becker, R.M. Clark, M.A. Deleplanque, R.M. Diamond, P. Fallon, L.P. Farris, E.A. Henry, J.R. Hughes, A.O. Macchiavelli, F.S. Stephens. *NIM*, **A354**, 591, (1995).
- [13] A. Neußer, H. Hübel, A. Al-Khatib, P. Bringel, A. Bürger, N. Nenoff, G. Schönwaßer et al., *Phys. Rev. C* 70, 064315 (2004).
- [14] J.F. Ziegler, J.P. Biersack and U. Littmark, *The Stopping and Ranges of Ions in Matter*, vol.1 (Pergamon, London 1985).
- [15] J.N. Wilson and B. Herskind, *NIM* **A455**, (2000), 612-619.
- [16] B. Herskind, G.B. Hagemann, G. Sletten, T. Døssing, C. Rønn Hansen, N. Schunck, S. Ødegaard, H. Hübel, P. Bringel et al. *Phys. Scr. T125*, (2006) 108.
- [17] T. Døssing, B. Herskind, S. Leoni, A. Bracco, R.A. Broglia, M. Matsuo and E. Vigezzi, *Physics Reports* **268** no.1, 1 - 84,(1996).